Available online at www.sciencedirect.com

ScienceDirect

Journal of Sound and Vibration 324 (2009) 74–90

JOURNAL OF SOUND AND VIBRATION

www.elsevier.com/locate/jsvi

An experimental study on transverse vibration of tapered bars in elasto-plastic regime

Debabrata Das, Prasanta Sahoo*, Kashinath Saha

Department of Mechanical Engineering, Jadavpur University, Kolkata 700032, India

Received 12 January 2009; accepted 22 January 2009
Handling Editor: L.G. Tham
Available online 17 March 2009

Abstract

In the present study, the natural frequencies of axially loaded, tapered bars are obtained experimentally. A tensile load is applied gradually till failure (necking) starts at the minimum cross-section end or yielding initiates at the maximum cross-section end. Experiments are carried out for aluminum and mild steel specimens with four different taper ratios. The results are presented in the amplitude–frequency plane as waterfall diagrams, which are processed further using a suitable windowing technique to better resolve the first two vibration modes. A comparison of experimental observations with results obtained from ANSYS indicates agreement in the elastic part of loading, but the results differ in the post-elastic domain. It is believed that the present results can serve as benchmarks for further investigation in this domain.

1. Introduction

Free flexural vibration analysis of axially loaded bars is an important area of research in the fields of mechanical, structural and aerospace engineering. Prediction of the dynamic behavior of such an axially loaded bar in the post-elastic state is quite a challenging and demanding task. Much research has been carried out in predicting the behavior of axially loaded bars under both compression and tension modes of loading. In post-elastic state, the dynamic behavior becomes completely different. The next few paragraphs provide a detailed account of the research work related to this field. The literature review also encompasses the work in the field of buckling just to signify and document the post-elastic behavior of bars and beams.

Karagiozova and Jones [1] studied numerically the dynamic elasto-plastic buckling phenomenon of rods under axial impact considering both axial and lateral inertia. Lepik [2] analyzed the dynamic buckling of elasto-plastic beams using linear strain hardening material behavior and extended the same to incorporate the effect of axial stress waves [3]. In an earlier study, Lepik [4] used an energy approach based on Hamilton's principle for a bifurcation analysis of an elasto-plastic beam. The dynamic elasto-plastic buckling phenomenon of square tube under axial impact has been studied by Karagiozova [5] and Karagiozova and Jones [6] considering isotropic linear strain hardening material behavior and using the von Mises yield

---

*Corresponding author. Tel./fax: +91 33 2414 6890.
E-mail address: psahoo@vsnl.net (P. Sahoo).

0022-460X/$ - see front matter © 2009 Elsevier Ltd. All rights reserved.
doi:10.1016/j.jsv.2009.01.047

criterion. Kong et al. [7] presented the static and dynamic analysis of Bernoulli–Euler beams based on strain gradient theory using both analytical and variational methods. Ma et al. [8] investigated dynamic instability of elastic–plastic beam using a three-degree-of-freedom beam model.

Ross and Johns [9] reported theoretical and experimental observations for plastic axisymmetric buckling of thin-walled conical and cylindrical shells under uniform external pressure. Zeinoddini et al. [10,11] studied the effects of pre-loading on the dynamic behavior of tubular and solid cylindrical structural elements using a commercial finite element package incorporating geometric and material nonlinearities and validated the simulation results with experimental results. Zhang et al. [12] presented a new algorithm based on a parametric variational principle for the simulation of dynamic elasto-plastic strain hardening/softening problems. Plaut and Virgin [13] investigated the stability and vibration characteristics of a flexible and inextensible half loop under self-weight for both linearly elastic and softening materials. Virgin and Plaut [14] carried out similar work for a column with initial curvature under self-weight.

Lacarbonara et al. [15] presented a nonlinear control strategy for the cancellation of principle-parametric resonance of the first skew-symmetric mode of a simply supported uniform elastic beam subjected to an axial end force. Jaworski and Dowell [16] considered the accuracy and convergence of the Rayleigh–Ritz method, component modal analysis and finite element method using ANSYS for the free vibration analysis of a cantilevered beam with multiple steps in cross-section. They also carried out an experiment to validate the predicted results. Li [17] presented general solutions for free vibration of multistep nonuniform beams with several concentrated masses, rotational springs and transitional springs attached at the ends and intermediate points.

Pulngern et al. [18] investigated large amplitude vibrations of horizontal variable arc length beams using the finite element method, and considering the effect of large initial static sag deflections due to self-weight. They have complemented the analytical results with results obtained from an experimental modal analysis. Jaroszewicz and Zoryi [19] employed the method of influence functions to solve the free transverse vibration problems of a vertical cantilever and a bar subjected to axial loads. The nonlinear dynamics of a pin-ended elasto-plastic beam with both kinematic and isotropic hardening has been discussed by Savi and Pacheco [20] using an iterative numerical procedure, and the results indicated practical problems in predicting the response of the beam. Recently, the present authors [21] have analyzed numerically the free vibration behavior of axially loaded nonuniform tapered bars in the elasto-plastic domain.

The literature review reveals that no experimental work is available for investigation of post-elastic dynamic behavior of an axially loaded, tapered bar. The available studies are devoted to calculating either the linear natural frequencies or the loaded natural frequencies in the elastic regime. In the present study experiments are carried out for two different bar materials and for four different taper ratios. Results are presented as waterfall plots obtained by improving the resolution of the experimentally acquired signal using a suitable windowing technique, for which a separate algorithm has been developed. The experimental results are also presented in a traditional load–frequency plane to compare with the simulation results generated using the commercial finite element package ANSYS (version 8.0).

2. Specimen description

2.1. Geometry

Two different materials, namely, aluminum and mild steel, are used in the present experimentation. For each material, four different types of tapered geometries are considered by varying the diameter of the specimen at the smaller end keeping the diameter at the larger end fixed. The schematic diagram of the specimen geometry is shown in Fig. 1. The various dimensions of the specimens are mentioned in Table 1.

2.2. Material properties

Using the ASTM standard (E08M) procedure, the stress–strain behavior is determined by the Instron testing machine. Strain is obtained directly using extensometer provided with the instrument, and the corresponding stress value is derived mathematically by dividing the corresponding applied load with the

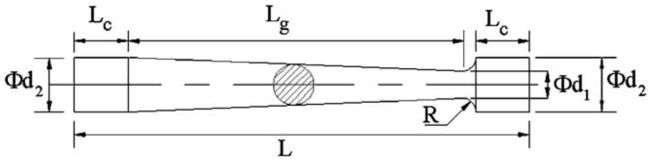

Fig. 1. Schematic diagram of specimen geometry.

Table 1
Specimen dimensions in mm.

Sl. no.	L	L_g	L_c	d_2	d_1	R	Material	Nomenclature
1	165	100	30	10±0.1	9±0.1	5	Aluminum Mild steel	AL1 MS1
2	165	100	30	10±0.1	8±0.1	5	Aluminum Mild steel	AL2 MS2
3	165	100	30	10±0.1	7±0.1	5	Aluminum Mild steel	AL3 MS3
4	165	100	30	10±0.1	6±0.1	5	Aluminum Mild steel	AL4 MS4

Notations shown in Fig. 1.

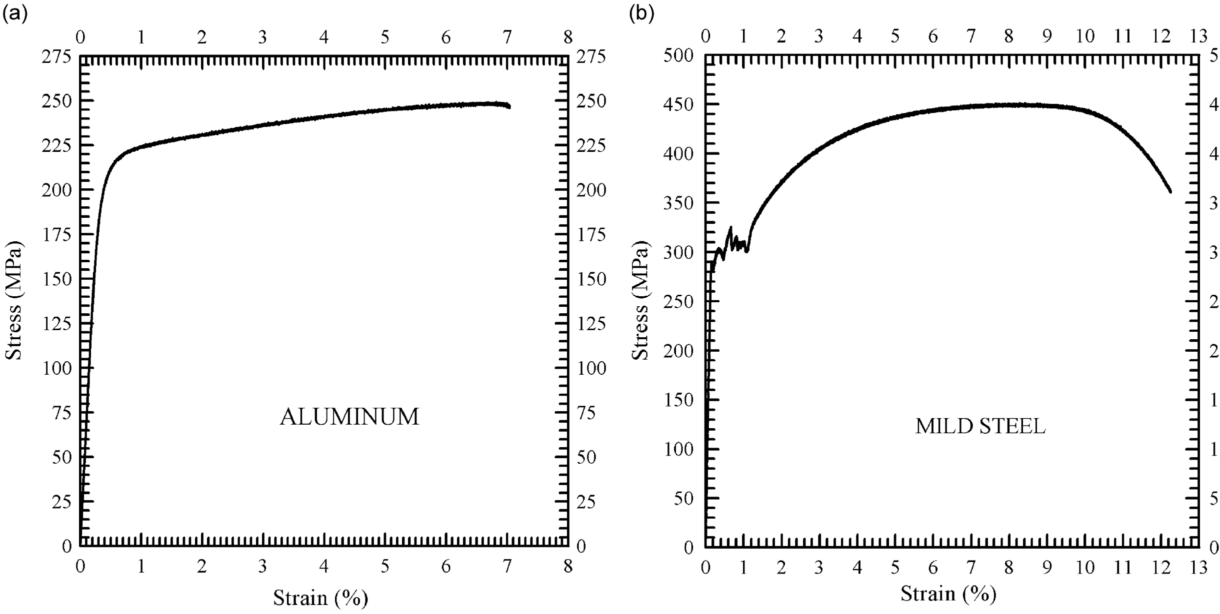

Fig. 2. Stress–strain diagrams: (a) aluminum and (b) mild steel.

specimen cross-sectional area. At the end of the experiment, the set of data for strain and stress is obtained in sequential file format. The Instron also provides the salient information of the stress–strain diagram, namely, yield stress (0.002 offset), ultimate tensile strength and elastic modulus. The information for yield strength and tensile strength are required for the dynamic test for controlling the load, whereas, the same information along with the elastic modulus are required for theoretical simulation. The engineering stress–strain diagram obtained for aluminum and mild steel are shown in Fig. 2(a) and (b), respectively.

3. Experimental details

3.1. Experimental set-up

A schematic diagram and a photograph of the experimental set-up are shown in Figs. 3 and 4, respectively. The set-up consists of five major components, namely, the accelerometer, coupler for the accelerometer, oscilloscope, computer and loading instrument.

The accelerometer (make: Kistler, type: 8728A500, acceleration range: $\pm 5000\,\mathrm{m/s^2}$, frequency range: 1 Hz–10 kHz) is mounted on the specimen using Petro-Wax adhesive material. To avoid the effect of mass loading, the weight of the accelerometer (1.6 g) is kept less than 10 percent the weight of the test specimen.

The coupler (make: Kistler, type: 5114, frequency range: 0.07 Hz–60 kHz) provides the electrical interface between the low-impedance, voltage mode piezoelectric sensor and the display or the recording instrument. The coupler has two functions: first, to provide constant current power supply to the impedance converter of the accelerometer; and second, to decouple the DC bias voltage from the output signal.

A digital storage oscilloscope (make: Tektronix, model: TDS 210) with a TDS2MM extension module for Fast Fourier Transform (FFT) is used to display, process and store the signal of the vibrating specimen. It has the following specifications: peak detect bandwidth: 50 MHz; sample rate range: 50 samples/s–1 Gigasamples/s; record length: 2500 samples; and lower frequency limit: 10 Hz. It has RS-232 port compatibility by which it is connected to a computer to transfer data.

A desktop computer with an Intel Pentium 4 CPU 2.40 GHz processor is used as the storage and (offline) processing device for the acquired data. Data acquired through the RS-232 communication port is grabbed by

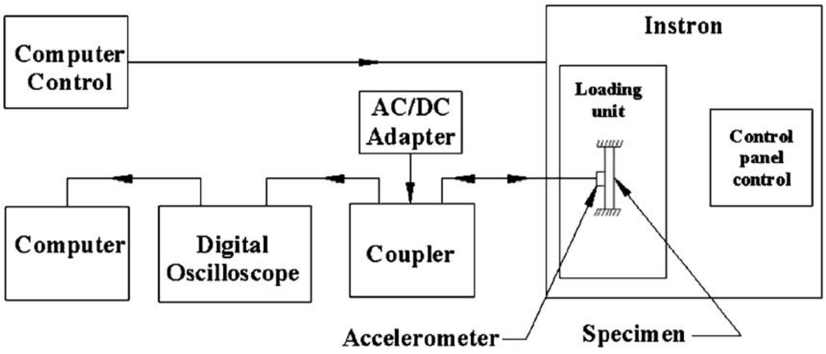

Fig. 3. Schematic diagram of the experimental setup.

Fig. 4. Photograph of the experimental setup.

the computer main memory using WSTRO Wavestar software. The software has the capability to process the saved data in offline mode and convert it into a sequential data format for further processing.

For loading purposes, a very robust servo hydraulic machine is used (make: Instron, model: 8801, maximum load capacity: ±100 kN and maximum axial movement: 150 mm). The inbuilt Bluehill software for online processing is used during the material testing to obtain the salient points in the stress–strain diagram and the material properties. The machine has two different independent modes of control for loading. One is computer control into which loading information can be provided using the Bluehill software interface. The other one is the manual mode in which the loading is controlled by a key in the control panel; this mode is used for the dynamic experiment.

3.2. Test procedure

Tests are carried out to determine the loaded natural frequencies of uniform tapered bars. The applied load is controlled in such a way that the bar enters its post-elastic state and finally failure (necking) occurs in the material. It is apparent that yielding initiates at the end of minimum cross-section, and with gradual increase in load, the yield front proceeds to form a yield region in the post-elastic state. Two cases are possible, either necking starts at the minimum cross-section before the yield front reaches the other end (maximum cross-section), or, the yield front reaches the maximum cross-section before necking starts at the critical section. Occurrence of a particular case depends on the yield strength and tensile strength as well as the ratio of diameters of maximum and minimum cross-section of the test specimen. As the material properties and the dimensions of the specimen are known, the approximate uniaxial load at which necking starts (P_u) at the minimum cross-section or yielding front reaches at maximum cross-section (P_{y2}) can be calculated theoretically. Accordingly load increment is controlled and end of test is confirmed. Various important load values are tabulated in Table 2, where, P_{y1} and P_{y2} are the loads at which yielding initiates at the minimum cross-section and yielding front reaches the maximum cross-section, respectively; P_u is the load at which necking starts at minimum cross-section.

The test procedure is as follows. First, the Instron is made ready for the operation after necessary initializations in accordance with the operating instructions. Using the computer control mode and by keeping the load protect capability of Instron 'on' (with a specified load), the test specimen is gripped in between the jaws (hydraulically). This is required to protect the specimen from overloading at the gripped ends. After the specimen is gripped, the load protect capability is made 'off' and the control is transferred to a control panel. Due to gripping, the test specimen is loaded by a small amount and the amount of load is shown in the load pane of the control panel. Depending on the magnitude and direction of initial loading, the specimen is given a small displacement by rotating the displacement key in the direction opposite to that of loading to nullify the effect of initial loading as much as possible. In addition, the Instron has the capability to compensate for the effect of pre-loading at the gripped ends to some extent.

Table 2
Important load values.

Material	Number	P_{y1} (kN)	P_{y2} (kN)	P_u (kN)
Aluminum	1	13.55	16.73	15.84
	2	10.71	16.73	12.52
	3	8.20	16.73	9.58
	4	6.02	16.73	7.04
Mild steel	1	17.81	21.99	28.69
	2	14.07	21.99	22.67
	3	10.78	21.99	17.36
	4	7.92	21.99	12.75

The accelerometer is mounted on the test specimen at a pre-defined location using adhesive. The location is selected in such a way that no node exists at that location for the first few (at least 4) mode shapes. The oscilloscope and coupler are powered on and 'math' mode is kept on with 'auto' trigger mode.

Table 3
Loads corresponding to load plane numbers.

Load plane number	Load (kN)							
	Aluminum				Mild steel			
	1	2	3	4	1	2	3	4
1	0.488	0.104	0.100	0.230	1.162	0.270	1.016	0.631
2	1.032	0.874	0.517	1.006	1.922	1.576	1.506	1.440
3	1.796	1.435	0.942	1.520	2.727	2.011	2.085	2.900
4	2.382	2.044	1.412	2.014	3.569	2.833	2.649	2.149
5	3.011	2.581	2.014	2.515	4.023	3.581	3.578	3.567
6	3.660	3.159	2.451	2.991	4.722	4.214	4.175	4.381
7	4.260	3.888	2.986	3.501	5.083	5.133	4.879	5.043
8	4.694	4.371	3.473	4.049	5.776	5.955	5.455	5.492
9	5.104	5.025	4.015	4.531	6.158	5.676	6.019	6.263
10	5.515	6.025	4.420	5.289	6.771	7.311	6.480	7.065
11	5.994	6.479	4.927	5.506	8.257	7.976	7.080	7.883
12	6.417	7.021	5.476	5.697	8.926	8.807	7.721	8.237
13	6.902	7.584	5.929	5.826	9.727	9.529	8.278	8.394
14	7.438	8.055	6.216	5.991	11.560	10.420	8.761	8.650
15	7.774	8.611	6.484	6.121	12.060	11.370	9.120	9.158
16	8.254	8.917	6.823	6.297	12.920	12.320	9.926	9.384
17	8.619	9.076	7.125	6.398	13.390	13.200	10.320	9.792
18	9.000	9.172	7.474	6.528	13.830	13.720	10.520	10.070
19	9.447	9.315	7.693	6.723	14.670	13.840	10.810	10.930
20	10.030	9.498	7.758	6.867	15.080	14.170	11.030	10.960
21	10.440	9.659	7.968	6.994	15.790	14.270	11.370	11.630
22	10.890	9.773	8.072	–	16.250	14.360	11.670	11.850
23	11.310	9.872	8.165	–	16.870	14.410	11.870	12.660
24	11.700	9.996	8.269	–	17.150	14.500	12.080	–
25	12.060	10.120	8.461	–	17.820	14.890	12.130	–
26	12.280	10.260	8.612	–	17.950	15.080	12.200	–
27	12.360	10.390	8.732	–	18.120	15.320	12.470	–
28	12.470	10.470	8.825	–	18.380	15.470	12.820	–
29	12.650	10.590	8.948	–	18.440	15.740	13.470	–
30	12.750	10.690	9.072	–	18.580	15.890	13.650	–
31	12.920	10.780	–	–	18.660	15.910	13.920	–
32	13.040	10.920	–	–	18.830	16.600	14.480	–
33	13.190	11.000	–	–	19.210	17.200	14.740	–
34	13.320	11.130	–	–	19.510	17.550	15.050	–
35	13.410	11.260	–	–	19.880	18.100	15.500	–
36	13.480	11.310	–	–	20.160	18.920	15.640	–
37	13.630	11.610	–	–	20.370	20.600	15.890	–
38	13.760	11.710	–	–	20.760	–	–	–
39	13.820	11.990	–	–	21.220	–	–	–
40	13.960	12.150	–	–	21.590	–	–	–
41	14.090	–	–	–	21.650	–	–	–
42	14.190	–	–	–	22.120	–	–	–
43	14.310	–	–	–	22.410	–	–	–
44	14.340	–	–	–	22.660	–	–	–
45	14.610	–	–	–	22.770	–	–	–
46	14.850	–	–	–	22.830	–	–	–
47	–	–	–	–	23.100	–	–	–

The load increment is prescribed by controlling the displacement key of the control panel of Instron manually to take the load to a higher value and it is kept static at that value. The oscilloscope is kept ready at the 'RUN' condition. The specimen is hammered to provide disturbance and the oscilloscope captures the signal from the vibrating specimen and plots FFT. Using the RS-232 communication port, data is sent and grabbed in the computer main memory using WSTRO Wavestar software, and it is stored in the secondary memory using an appropriate file name and format. These steps are repeated until the desired load to be applied is reached or failure occurs in the specimen.

4. Results and discussions

The dynamic behavior of tapered bars in terms of loaded natural frequency for the first two modes is obtained using the procedure mentioned in Section 3.2. FFT capability of the extension module of the oscilloscope transformed the signal of the vibrating specimen from time domain to frequency domain, which is acquired and stored in the computer. The dynamic behavior for different loads is shown as 3D waterfall plots generated in MATLAB. In these plots, the frequency–amplitude planes are plotted one after another with increasing values of loads. A sequentially assigned load plane number is used to identify each frequency–amplitude plane. Although the load plane number acts as an indicator of load increments, a uniform increment could not be given during the experiment. The values of loads corresponding to load plane numbers are shown in Table 3. For each specimen, data are captured within frequency range of 0–25.5 kHz. The waterfall plots in the full frequency range are presented first with the data obtained directly from the oscilloscope. Subsequently, different waterfall plots are then magnified for each mode as observed from the full frequency range plot.

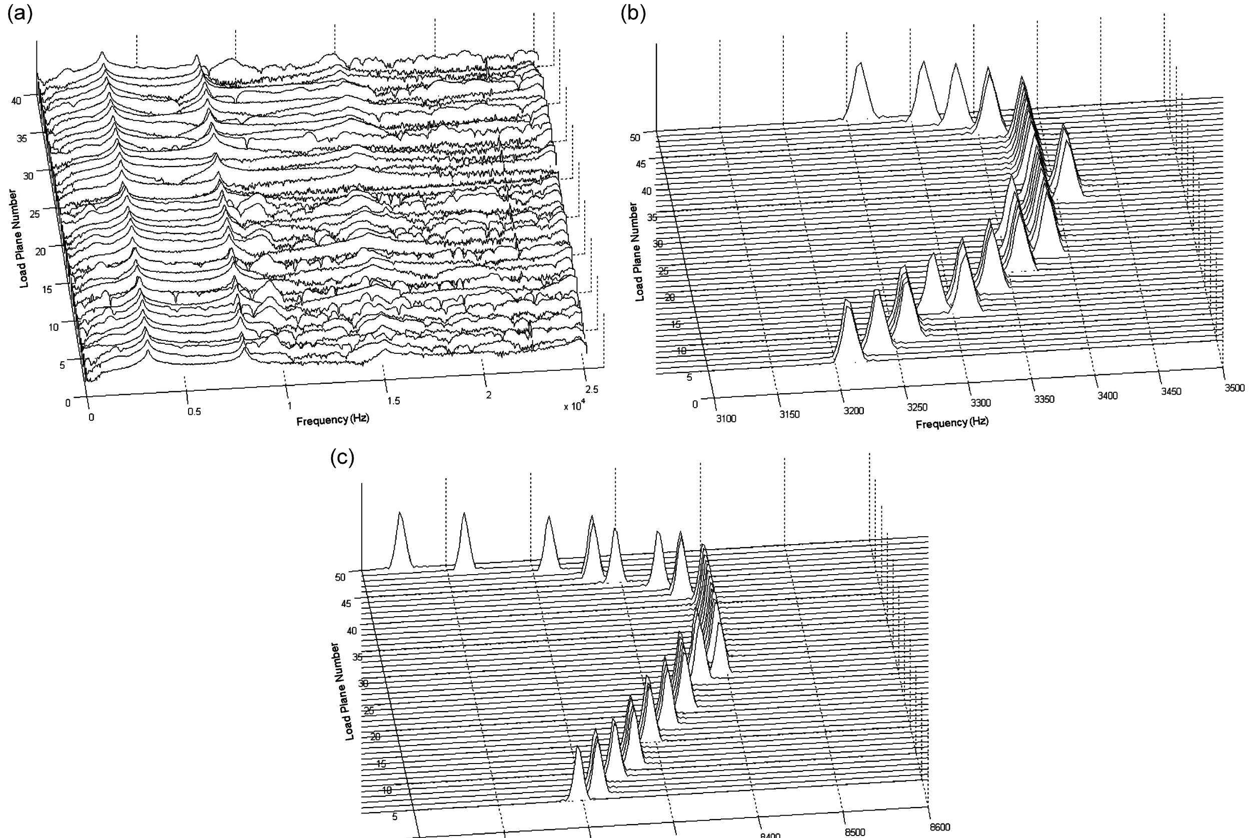

Fig. 5. Waterfall plots for AL1: (a) full frequency range, (b) first vibration mode and (c) second vibration mode.

To obtain the magnified waterfall plots for each mode of vibration, the original signal is further processed to improve resolution. The original signal obtained in the frequency domain undergoes certain leakage effects due to the error induced during FFT processing. This is why the peaks for each mode of vibration in the magnified waterfall plots do not seem to be sharp enough to produce better visibility. Thus, the original signal requires a windowing operation to be performed on it to regain sharper peaks and better visibility. It is well known that windowing can be performed on the signal either in the time or frequency domains. As the data acquired for the present experiment is in the frequency domain, windowing is performed in the frequency domain. The Hanning function was found to be suitable as the windowing function for the present case. The FFT of the Hanning function is performed once, stored in memory, and is then applied to each central frequency where windowing is needed. For each load plane, the central frequencies correspond to the peaks of each vibration mode. The detailed algorithm of windowing operation [22] is omitted here to maintain brevity.

Use of waterfall diagram for dynamic analysis of structural elements is quite useful. Kang and Raman [23] experimentally investigated the vibration and acoustic oscillation of disks rotating in an air-filled medium and presented some results in the form of waterfall diagrams. Wu and Meng [24] presented a method to identify rotor malfunction based on 3D spectrum analysis and extensively used waterfall diagrams. In the present study, the 2D load–frequency plots are also obtained for each specimen from waterfall diagrams. The frequencies for each mode of vibration corresponding to each load are extracted from the original diagram using a separate numerical algorithm [22] to present a comparison of the experimental results with the simulation plots obtained using ANSYS.

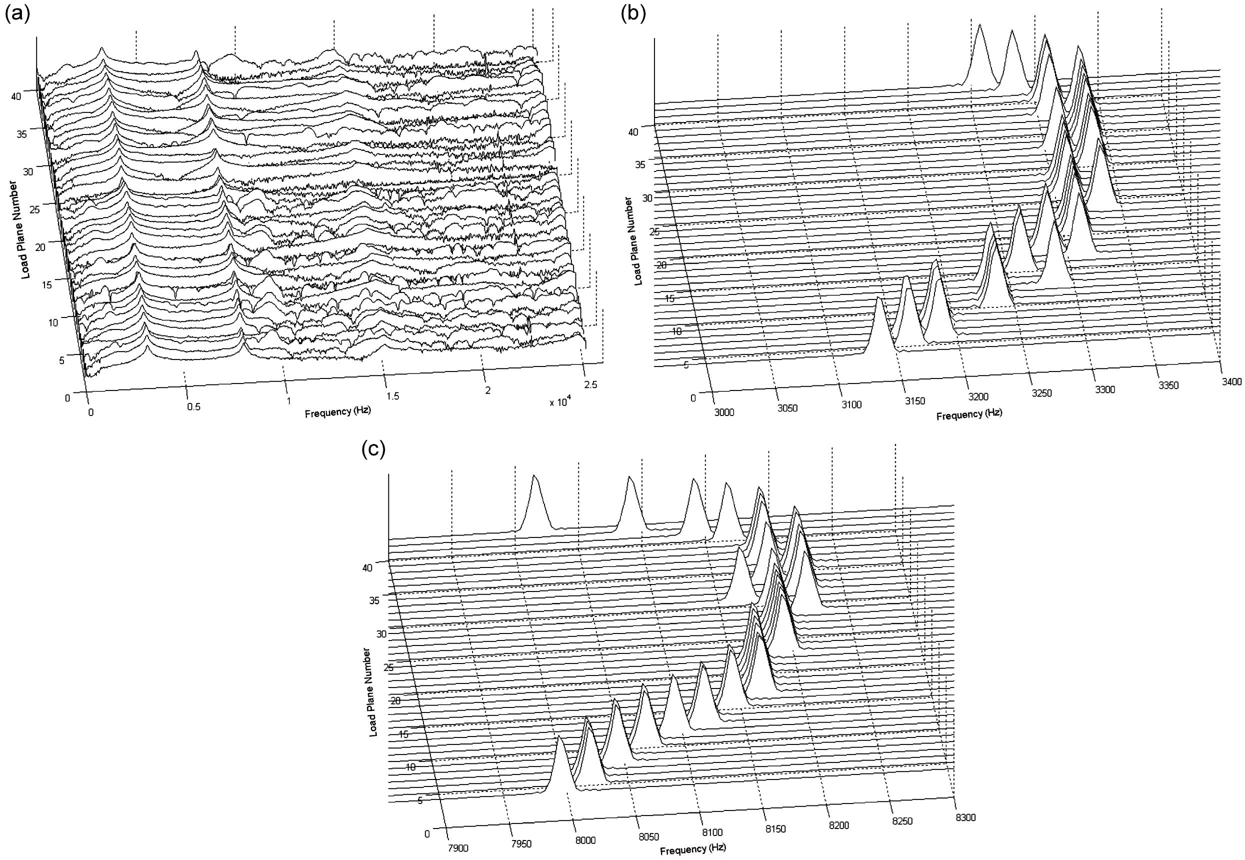

Fig. 6. Waterfall plots for AL2: (a) full frequency range, (b) first vibration mode and (c) second vibration mode.

4.1. Results for aluminum

It is well known that each structural element has its own natural frequencies for different modes of vibration, and the free vibration behavior changes appreciably when the structural element is loaded externally. The natural frequency of such a member is called the loaded natural frequency. The loaded natural frequency increases for tensile and reduces for compressive axial loadings. However, when the induced stress exceeds the yield limit, i.e., when plastic flow commences, the material properties no longer remain uniform throughout the test specimen. Due to the gradual increase in load, a region in a post-elastic state develops where materials are at different post-yield levels. The growth of this region causes softening of the tapered bar as its stiffness reduces when compared to the purely elastic state of the material. The present paper investigates how the tapered bar behaves dynamically in a post-elastic state.

Fig. 5(a) presents the waterfall plot for aluminum specimen AL1 for the full frequency range. Magnified plots of the first and second vibration modes are shown separately in Fig. 5(b) and (c), respectively. Fig. 5(a) is obtained from the original signal whereas Fig. 5(b) and (c) are obtained with Hanning windowing operation performed on the original signal as explained earlier. Figs. 6–8 present similar plots for aluminum specimens AL2, AL3 and AL4, respectively. In some of the magnified waterfall plots, some peaks are obtained which are out of the general trend. These outliers are probably obtained as a consequence of the high noise level comparable with the amplitude of the actual harmonics.

The general trend for each vibration mode is that the frequency of vibration increases with tensile load, with a decreasing slope in the elastic region. However, as the load magnitude is increased further to initiate plastic deformation in the material, the free vibration frequency decreases sharply and becomes sharper for higher vibration modes. Exception to this observation is observed for specimen AL4, for which the frequency of

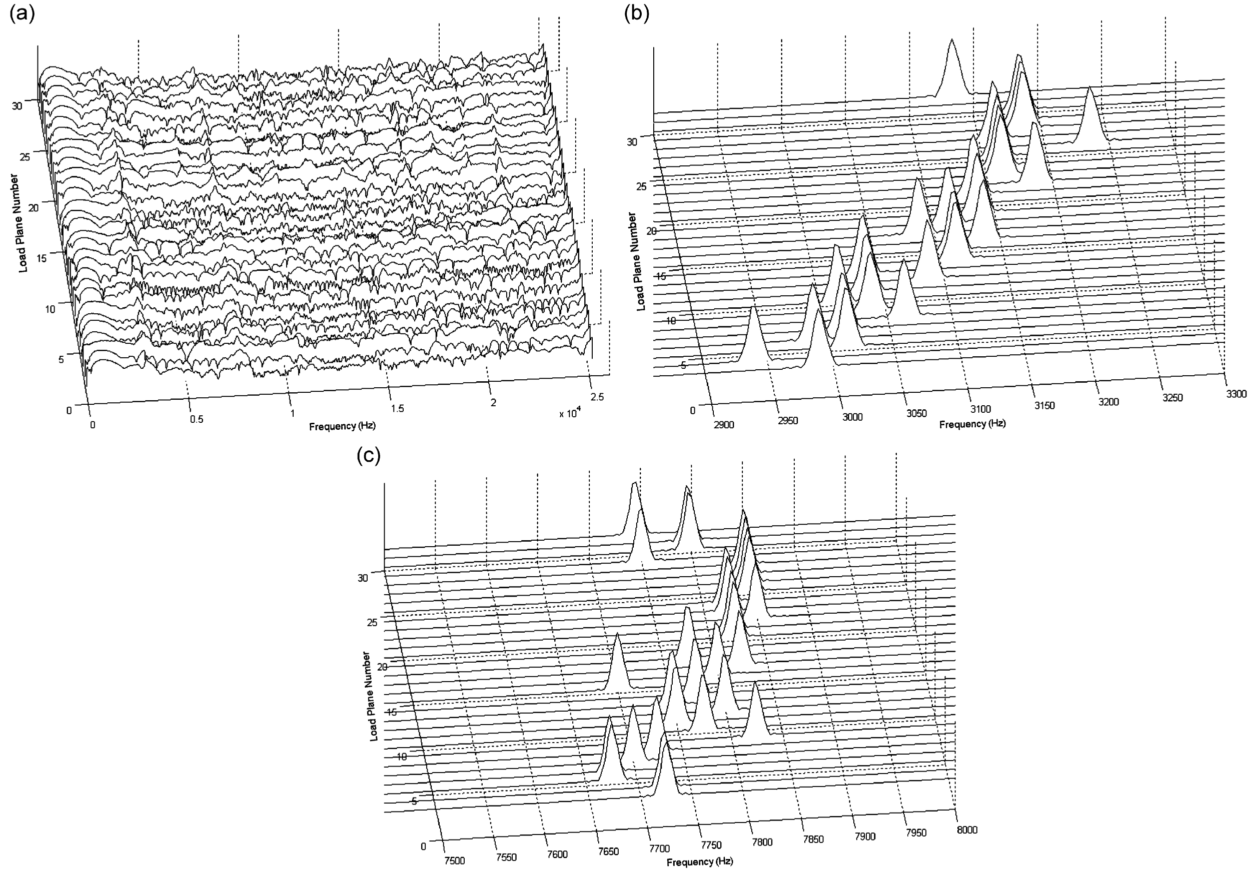

Fig. 7. Waterfall plots for AL3: (a) full frequency range, (b) first vibration mode and (c) second vibration mode.

vibration continues to increase after the inception of plastic deformation. The load plane number corresponding to the commencement of plastic deformation for each specimen can be obtained from Tables 2 and 3. This change in behavior with taperness ratio is probably due to the dominance of stretching effect

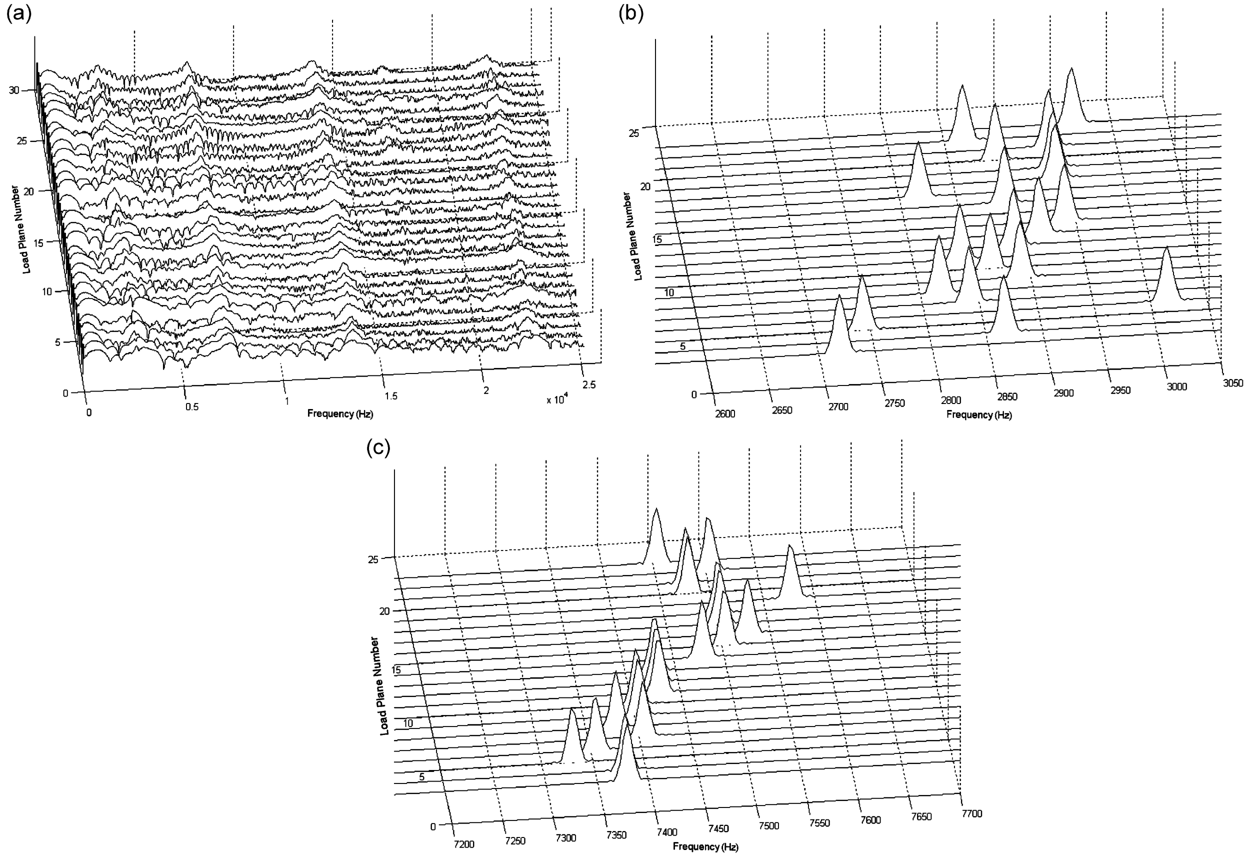

Fig. 8. Waterfall plots for AL4: (a) full frequency range, (b) first vibration mode and (c) second vibration mode.

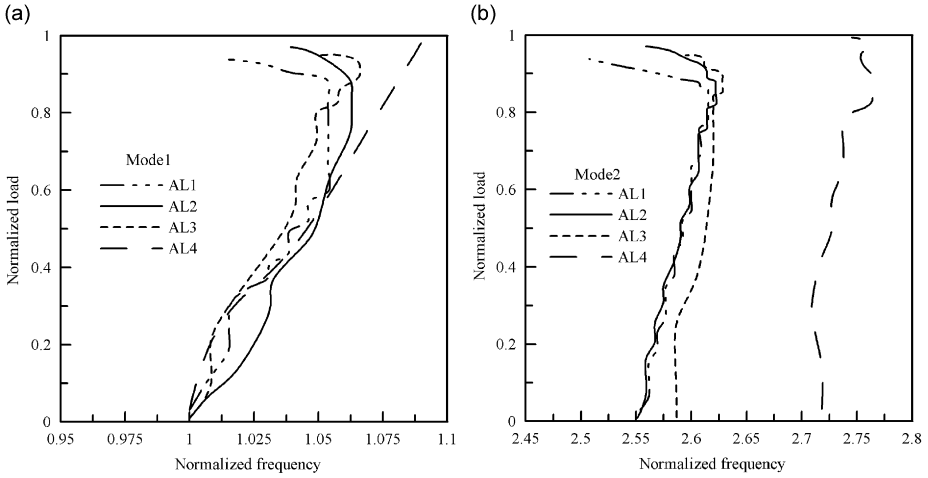

Fig. 9. Two-dimensional plots in normalized load–frequency plane for aluminum: (a) first vibration mode and (b) second vibration mode.

over the softening effect due to plastic deformation. It is also seen that as the taperness of the bar increases (from AL1 to AL4), the frequency of vibration in the unloaded condition decreases considerably.

To visualize the comparative dynamic behavior of different aluminum specimens, 2D load–frequency plot in normalized plane for aluminum specimens, obtained using the peaks from Figs. 5(b), 6(b), 7(b) and 8(b), is presented in Fig. 9(a) for first vibration mode. Similar plot for second vibration mode, obtained using the peaks from Figs. 5(c), 6(c), 7(c) and 8(c), is presented in Fig. 9(b). It is to be noted that, load is normalized by P_u,

Fig. 10. Finite element model of aluminum specimen.

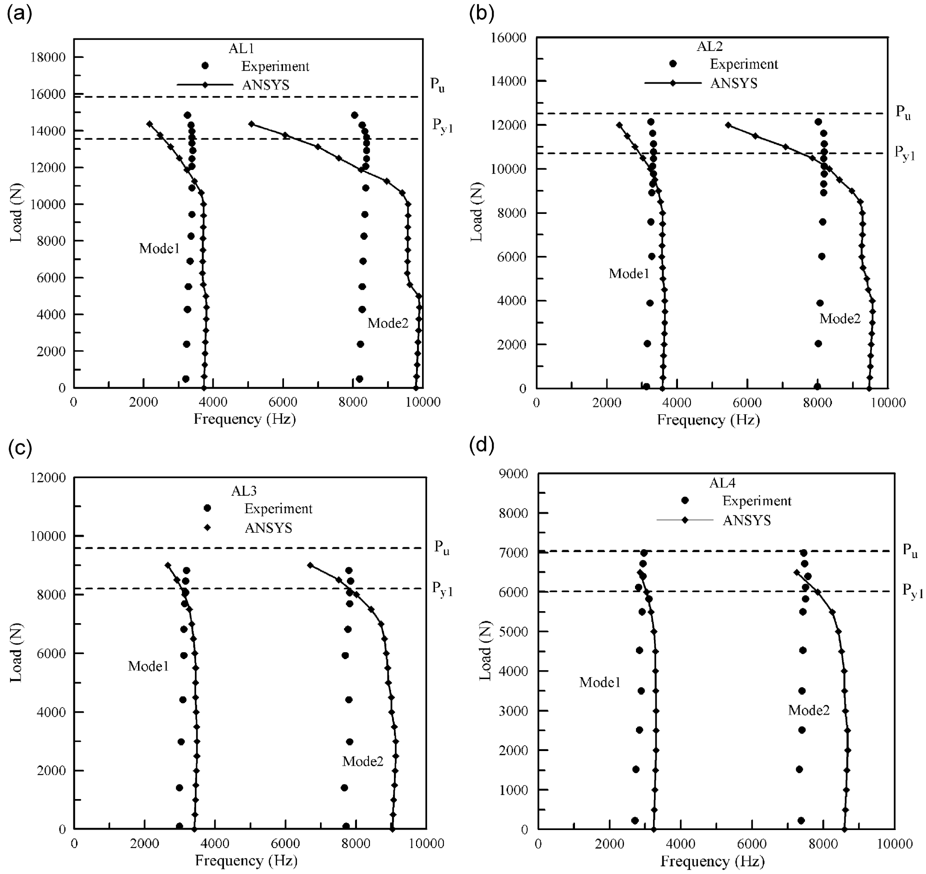

Fig. 11. Comparison plots in load–frequency plane: (a) AL1, (b) AL2, (c) AL3 and (d) AL4.

the load at which necking starts at minimum cross-section, and frequency is normalized by the unloaded frequency. The plots shown in Fig. 9 are generated by fitting spline curves through the data points and removing the distinct outliers. The general trend in these figures indicates hardening–softening behavior as mentioned in the previous paragraph and the effect of taperness becomes obvious for specimen AL4, especially for the second vibration mode.

The experimental results are then compared with the numerical results obtained using ANSYS. The finite element model in ANSYS is built using SOLID 95 elements and the loaded natural frequencies are obtained using a pre-stressed modal analysis. Fig. 10 shows the finite element model of the tapered bar in meshed condition. The stress–strain data obtained during material testing are provided as input in the simulation study to match the exact material behavior. The simulated and experimental results are compared in Fig. 11(a)–(d) for AL1, AL2, AL3 and AL4, respectively. The important load values of the specimens are indicated in the plots by horizontal lines.

The comparison plots show that the experimental results match well with the simulation results for first vibration mode but a discrepancy arises for the second vibration mode. The discrepancy is apparent in the post-elastic region where the decrease in vibration frequency of the simulation results is sharper than that of the experimental results. The anomalous behavior of elastic–plastic beam dynamics under impulsive loading has also been reported by Li et al. [25]. There are different reasons that may explain this discrepancy. In the simulation study, a multilinear isotropic hardening model is used for the nonlinear material model, which may not match the actual material behavior. Secondly, during dynamic testing, the gripping of the specimen at the jaws produces significant pre-stressing and permanent deformation, which is not taken into account in the simulation model. Also, an altogether different physical phenomenon might exist which gives rise to the discrepancy in the dynamic behavior between the experimental and simulation results.

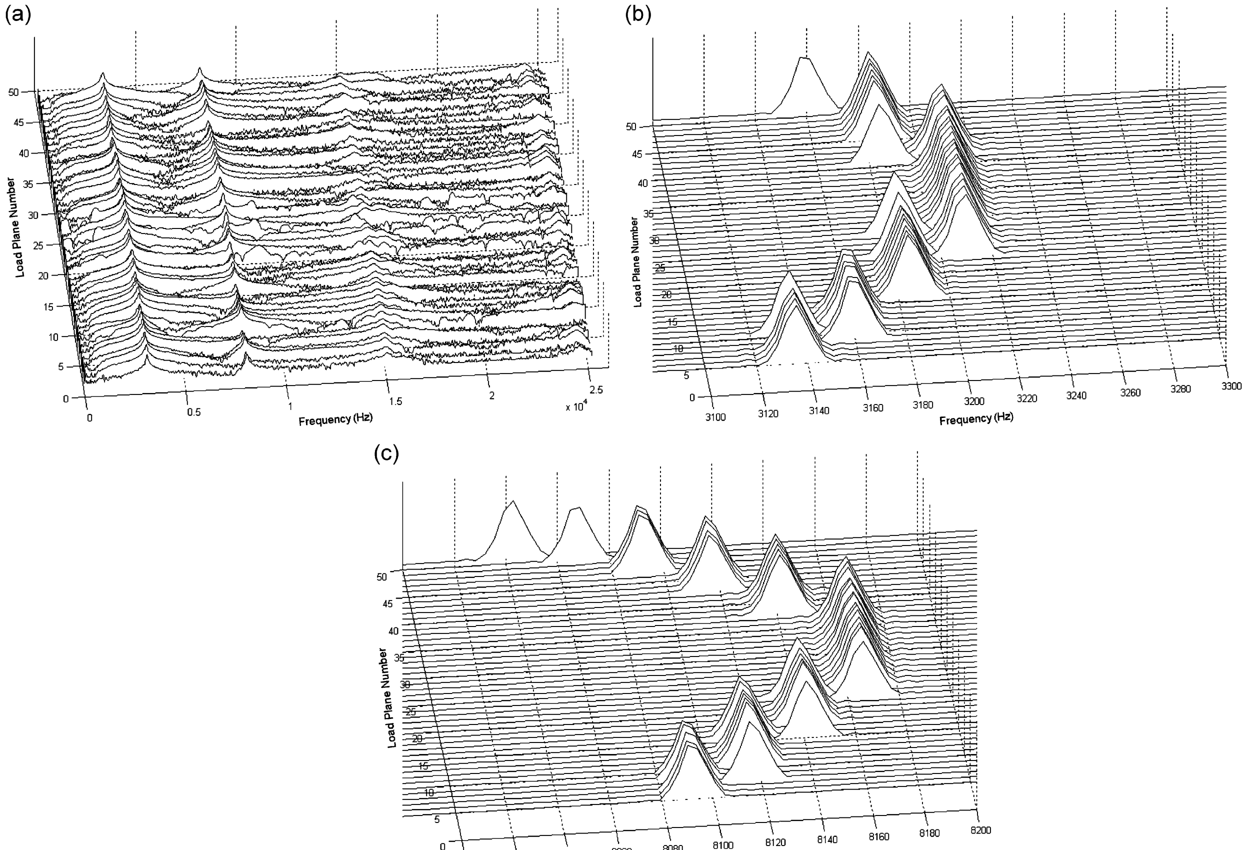

Fig. 12. Waterfall plots for MS1: (a) full frequency range, (b) first vibration mode and (c) second vibration mode.

4.2. Results for mild steel

Fig. 12(a) presents the waterfall plot for mild steel specimen MS1 for full frequency range. Magnified plots for the same specimen of first and second vibration modes are shown in Fig. 12(b) and (c), respectively. These plots are obtained with the Hanning windowing operation performed on the original signal as explained earlier. Figs. 13–15 present similar plots for mild steel specimens MS2, MS3 and MS4, respectively. Like the case for aluminum specimens, the high noise level induced some peaks which are out of the general trend in some of the magnified plots of mild steel specimens. The general trend observed for each vibration mode of mild steel specimens remains similar to that observed for aluminum specimens.

The comparative dynamic behavior of different mild steel specimens, in 2D normalized load–frequency plane, has been shown in Fig. 16(a) for first vibration mode and this plot is generated using the peaks from Figs. 12(b), 13(b), 14(b) and 15(b). Similar plot for second vibration mode, obtained using the peaks from Figs. 12(c), 13(c), 14(c) and 15(c), is presented in Fig. 16(b). The normalization schemes, as used for aluminum specimens, have been used for this case also. The plots shown in Fig. 16 are generated by removing the outliers and fitting splines through the data points. The general observations for this figure remain same as in the previous case for aluminum specimens.

The comparisons of the experimental results for mild steel specimens with the numerical results obtained using ANSYS are shown in Fig. 17(a)–(d) for MS1, MS2, MS3 and MS4, respectively. The finite element modeling and analysis procedure in ANSYS is same as mentioned for aluminum specimens. The stress–strain data for material property obtained during material testing are provided as input for the simulation study to match the exact material behavior. It may be noted that stress–strain diagram for mild steel (Fig. 2(b)) contains sharp peaks and discontinuities around the yield region, which makes the convergence for the

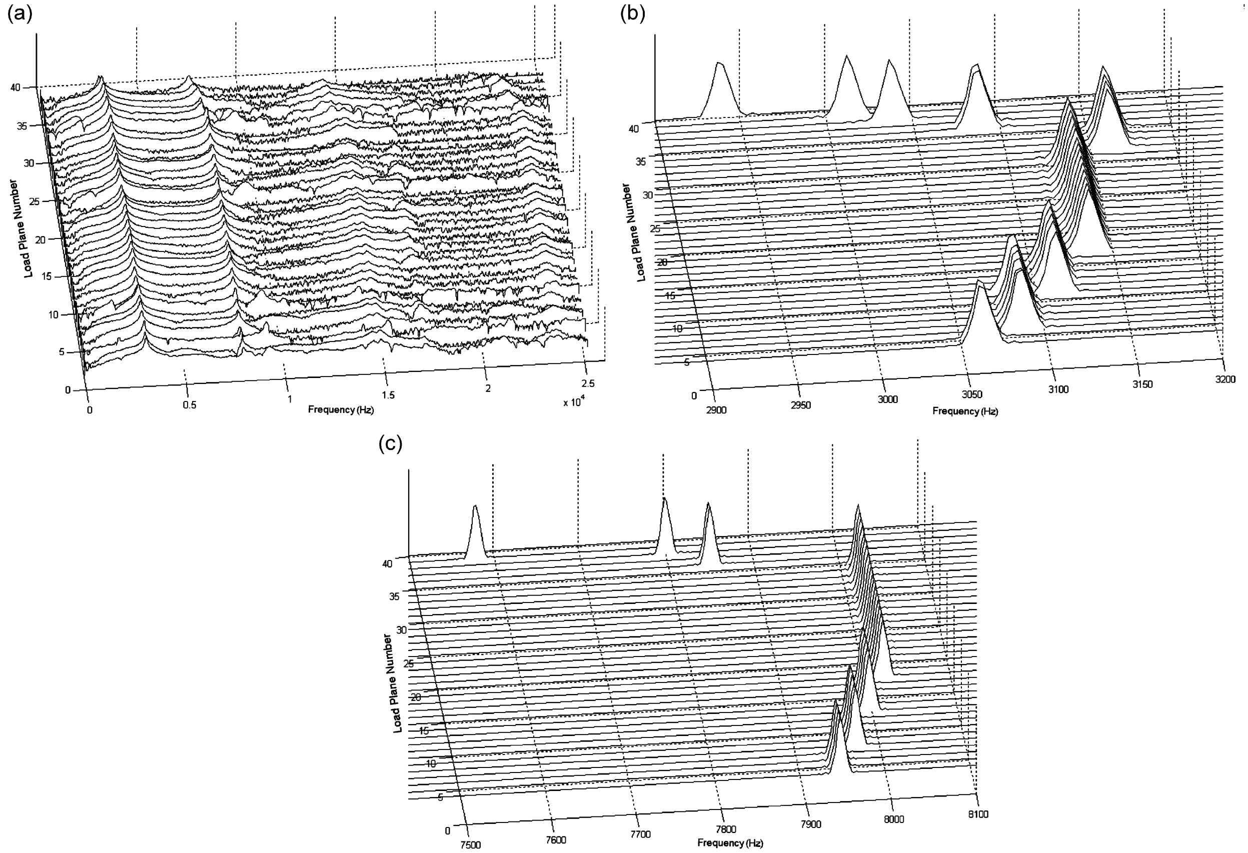

Fig. 13. Waterfall plots for MS2: (a) full frequency range, (b) first vibration mode and (c) second vibration mode.

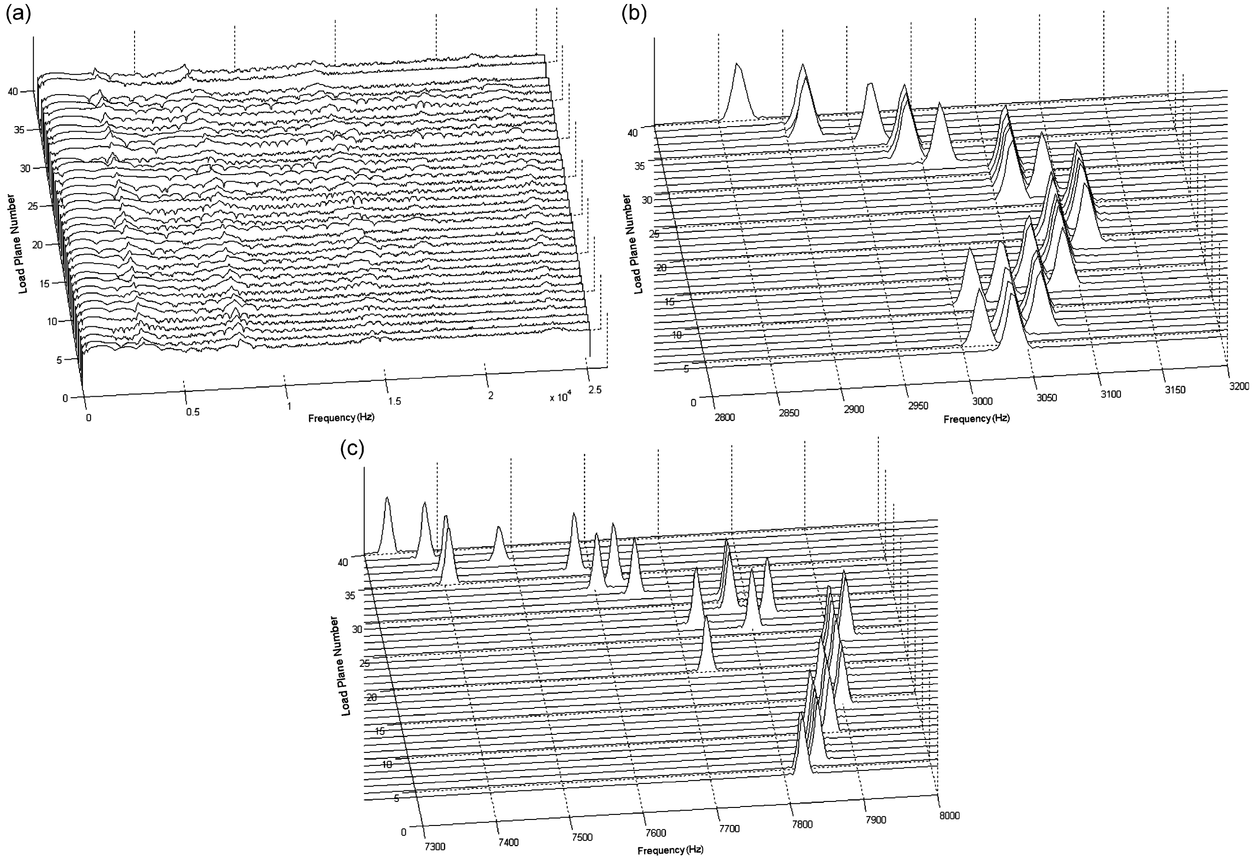

Fig. 14. Waterfall plots for MS3: (a) full frequency range, (b) first vibration mode and (c) second vibration mode.

simulation study almost impossible. To overcome this problem, a smooth stress–strain curve has been assumed around the yield region for the simulation study.

The comparison plots show that the loaded natural frequency trends for the experimental results match the simulation results within the elastic part of the loading, but a qualitative discrepancy prevails for higher modes. The reasons for this discrepancy are the same as those mentioned for aluminum specimens. Although the trends of the results are initially in good agreement, they begin to deviate when the load is increased further into the post-elastic domain.

The experimental findings are identical for both the mild steel and aluminum specimens. Each material's experimental results closely match with ANSYS for the first mode of transverse vibration and within elastic part of the loading. However, the higher mode results differ in magnitude of frequency as well as in nature in the post-elastic domain. This discrepancy opens up new avenues for future study in this direction. The present study considers tapered bars of circular cross-section only, and the effect of other specimen geometries is another area for future study.

5. Conclusions

The paper investigates experimentally the elastic and post-elastic free vibration behavior of axially loaded, tapered bars. Detailed descriptions of the experimental set-up and test procedure are presented, and a numerical algorithm for processing the acquired signal has been developed to obtain better resolution of the waterfall diagrams. Experimental work has been carried out on specimens having circular cross-section for two different materials, and the observations are found to be similar. A comparison between experimental observations and results simulated using the commercial analysis package ANSYS indicates good agreement

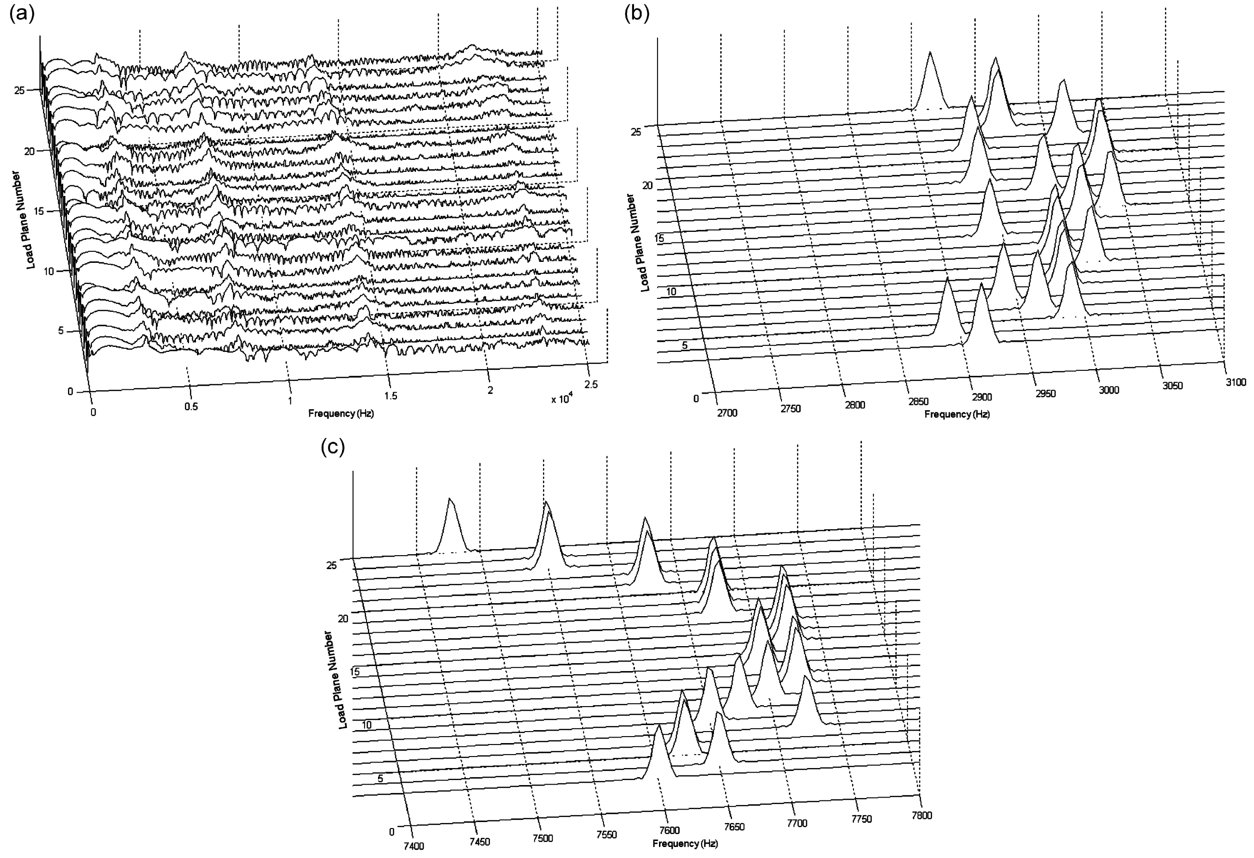

Fig. 15. Waterfall plots for MS4: (a) full frequency range, (b) first vibration mode and (c) second vibration mode.

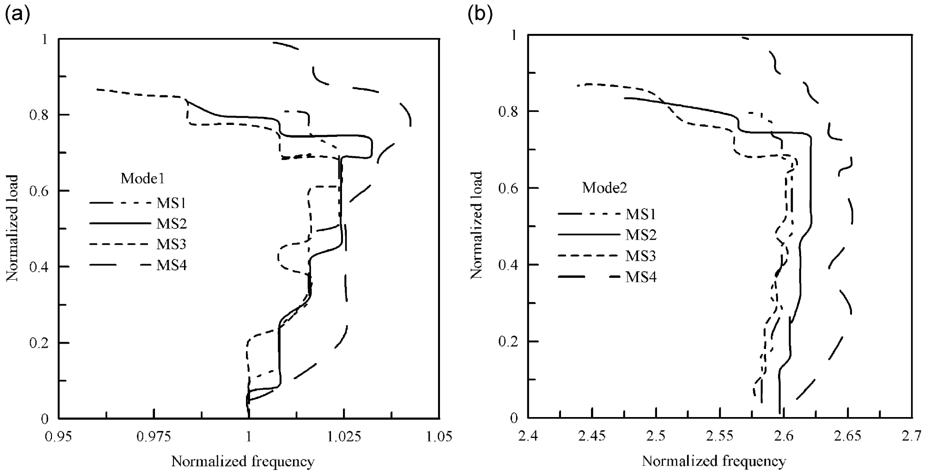

Fig. 16. Two-dimensional plots in normalized load–frequency plane for mild steel: (a) first vibration mode and (b) second vibration mode.

in the elastic part of loading, although the results differ when load is increased further in post-elastic domain. This observation points towards the inadequacy of the simulation models, and the suggested future work aims to improve the agreement of dynamic behavior between simulation and experiment of axially loaded, tapered bars in the post-elastic regime.

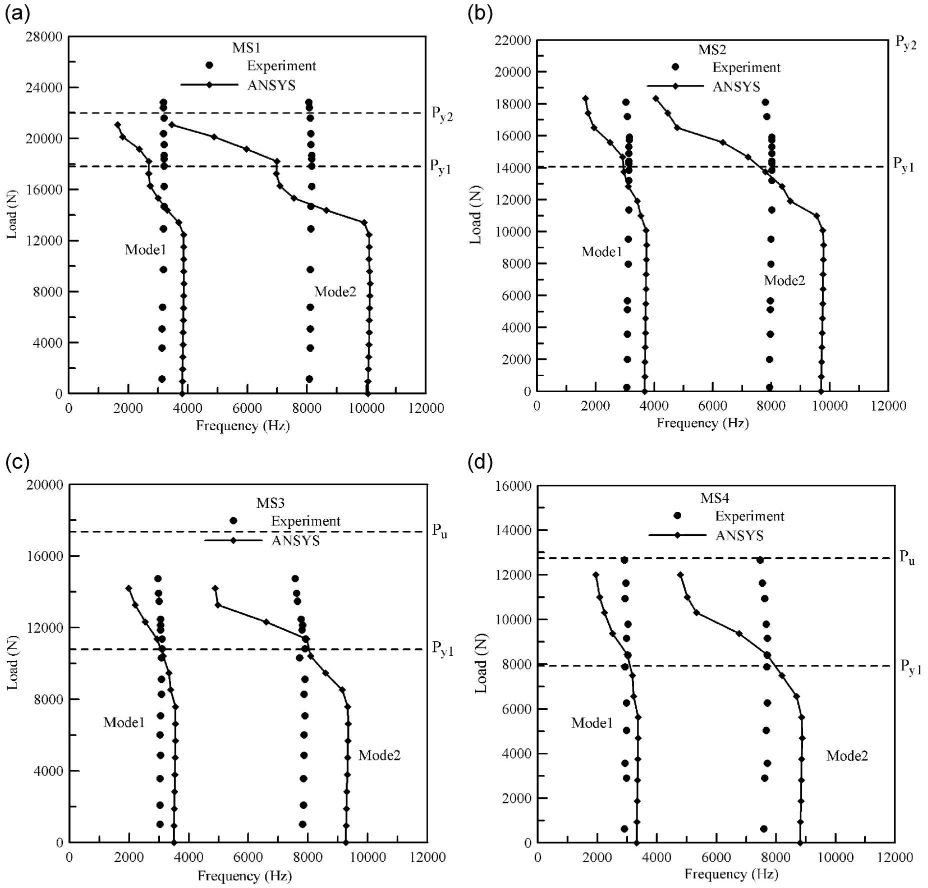

Fig. 17. Comparison plots in load–frequency plane: (a) MS1, (b) MS2, (c) MS3 and (d) MS4.

Acknowledgment

The authors are thankful to the anonymous reviewer, whose comments, suggestions and meticulous corrections in the original manuscript were instrumental towards improvement of the quality of the paper in its present form.

References

[1] D. Karagiozova, N. Jones, Dynamic elastic–plastic buckling phenomena in a rod due to axial impact, *International Journal of Impact Engineering* 18 (1996) 919–947.

[2] Ü. Lepik, On dynamic buckling of elastic–plastic beams, *International Journal of Non-Linear Mechanics* 35 (2000) 721–734.

[3] Ü. Lepik, Dynamic buckling of elastic–plastic beams including effects of axial stress waves, *International Journal of Impact Engineering* 25 (2001) 537–552.

[4] Ü. Lepik, A contribution to bifurcation analysis of elastic–plastic beams, *International Journal of Impact Engineering* 21 (1998) 35–49.

[5] D. Karagiozova, Dynamic buckling of elastic–plastic square tubes under axial impact—I: stress wave propagation phenomenon, *International Journal of Impact Engineering* 30 (2004) 143–166.

[6] D. Karagiozova, N. Jones, Dynamic buckling of elastic–plastic square tubes under axial impact—II: structural response, *International Journal of Impact Engineering* 30 (2004) 167–192.

[7] S. Kong, S. Zhou, Z. Nie, K. Wang, Static and dynamic analysis of micro beams based on strain gradient elasticity theory, *International Journal of Engineering Science*, doi:10.1016/j.ijengsci.2008.08.008.

[8] G.W. Ma, Y.M. Liu, J. Zhao, Q.M. Li, Dynamic instability of elastic–plastic beams, *International Journal of Mechanical Sciences* 47 (2005) 43–62.

[9] C.T.F. Ross, T. Johns, Plastic axisymmetric collapse of thin-walled circular cylinders and cones under uniform external pressure, *Thin-Walled Structures* 30 (1998) 35–54.

[10] M. Zeinoddini, J.E. Harding, G.A.R. Parke, Dynamic behavior of axially pre-loaded tubular steel members of offshore structures subjected to impact damage, *Ocean Engineering* 26 (1999) 963–978.

[11] M. Zeinoddini, J.E. Harding, G.A.R. Parke, Axially pre-loaded steel tubes subjected to lateral impacts (a numerical simulation), *International Journal of Impact Engineering* 35 (2008) 1267–1279.

[12] H. Zhang, X. Zhang, J.S. Chen, A new algorithm for numerical solution of dynamic elastic–plastic hardening and softening problems, *Computers & Structures* 81 (2003) 1739–1749.

[13] R.H. Plaut, L.N. Virgin, Three-dimensional postbuckling and vibration of vertical half-loop under self-weight, *International Journal of Solids and Structures* 41 (2004) 4975–4988.

[14] L.N. Virgin, R.H. Plaut, Postbuckling and vibration of linearly elastic and softening columns under self-weight, *International Journal of Solids and Structures* 41 (2004) 4989–5001.

[15] W. Lacarbonara, H. Yabuno, K. Hayashi, Non-linear cancellation of the parametric resonance in elastic beams: theory and experiment, *International Journal of Solids and Structures* 44 (2007) 2209–2224.

[16] J.W. Jaworski, E.H. Dowell, Free vibration of a cantilevered beam with multiple steps: comparison of several theoretical methods with experiment, *Journal of Sound and Vibration* 312 (2008) 713–725.

[17] Q.S. Li, An exact approach for free flexural vibrations of multistep non-uniform beams, *Journal of Vibration and Control* 6 (2000) 963–983.

[18] T. Pulngern, S. Chucheepsakul, M.W. Halling, Analytical and experimental studies on the large amplitude free vibrations of variable-arc-length beams, *Journal of Vibration and Control* 11 (2005) 923–947.

[19] J. Jaroszewicz, L. Zoryi, Investigation of the effect of axial loads on the transverse vibrations of a vertical cantilever with variable parameters, *International Applied Mechanics* 36 (2000) 1242–1251.

[20] M.A. Savi, P.M.C.L. Pacheco, Chaos and unpredictability in the vibration of an elasto-plastic beam, *Journal of the Brazilian Society of Mechanical Sciences* 23 (2001) 253–267.

[21] D. Das, P. Sahoo, K.N. Saha, Dynamic analysis of non-uniform taper bars in post-elastic regime under uniform axial loading, *Materials and Design*, doi:10.1016/j.matdes.2008.08.027.

[22] D. Das, P. Sahoo, K.N. Saha, A numerical algorithm for windowing operation on waterfall diagrams, *Proceedings of 53rd Congress of Indian Society of Theoretical and Applied Mechanics*, Hyderabad, India, 2008, pp. 158–163.

[23] N. Kang, A. Raman, Vibrations and stability of a flexible disk rotating in a gas-filled enclosure—part 2: experimental study, *Journal of Sound and Vibration* 296 (2006) 676–689.

[24] F.Q. Wu, G. Meng, Feature extraction based on the 3D spectrum analysis of acoustic signals to identify rotor malfunction, *International Journal of Advanced Manufacturing Technology* 28 (2006) 1146–1151.

[25] Q.M. Li, Y.M. Liu, G.W. Ma, The anomalous region of elastic–plastic beam dynamics, *International Journal of Impact Engineering* 32 (2006) 1357–1369.